

## Article

# Direct Tensile Capacity of Steel-Tube Connections in a Precast Concrete Double-Wall System

Didar Meiramov <sup>1</sup>, Yujae Seo <sup>1</sup>, Hyunjin Ju <sup>2,\*</sup>  and Hae-Chang Cho <sup>3</sup>

<sup>1</sup> Department of Architecture and Architectural Engineering, Hankyong National University, Jungang-ro 327, Anseong 17579, Gyeonggi, Republic of Korea; didar.meiramov@hknu.ac.kr (D.M.); tjdbwo@hknu.ac.kr (Y.S.)

<sup>2</sup> School of Architecture and Design Convergence, Hankyong National University, Jungang-ro 327, Anseong 17579, Gyeonggi, Republic of Korea

<sup>3</sup> Technology Center, Dream Structural Engineers Co., Ltd., Dontan-daero 21-gil 10, Hwaseong 18471, Gyeonggi, Republic of Korea; hc.cho@dreamse.co.kr

\* Correspondence: hju@hknu.ac.kr

**Abstract:** This study introduces a new precast concrete (PC) double-wall system designed to simplify the complex fabrication process of existing PC double-wall systems and eliminate laitance and other defects that can occur during the manufacture of concrete panels. An experiment and finite element analysis were conducted on 11 specimens to determine the tensile resistance performance of rectangular steel tubes that maintain spacing to avoid damage to the PC panels during transportation or on-site installation. Specimens varied in terms of the end details of the rectangular steel tubes, such as the presence of welded steel plates or embedded concrete and total length in terms of whether longer or shorter specimens were used. As a result, the specimens showed a 20–30% increase in maximum tensile strength compared to the control specimen according to the end details, except for the case where side steel plates were cut and bent inward. The control specimen filled with concrete was the most suitable for connections when constructing PC double-wall systems. It has significant tensile resistance according to the experiment and finite element analysis and does not require additional construction steps or costs.

**Keywords:** precast concrete; double-wall connection; steel tube; experiment; finite element analysis



**Citation:** Meiramov, D.; Seo, Y.; Ju, H.; Cho, H.-C. Direct Tensile Capacity of Steel-Tube Connections in a Precast Concrete Double-Wall System. *Buildings* **2023**, *13*, 2872. <https://doi.org/10.3390/buildings13112872>

Academic Editors: Fangwen Wu, Xiaohong Zheng, Yunchao Tang, Haibo Jiang and Renda Zhao

Received: 24 October 2023  
Revised: 13 November 2023  
Accepted: 15 November 2023  
Published: 16 November 2023



**Copyright:** © 2023 by the authors. Licensee MDPI, Basel, Switzerland. This article is an open access article distributed under the terms and conditions of the Creative Commons Attribution (CC BY) license (<https://creativecommons.org/licenses/by/4.0/>).

## 1. Introduction

Building a precast concrete (PC) double-wall system involves fabricating two concrete panels in a factory, connecting them vertically or horizontally with reinforcing steel, and then completing the wall structure by placing concrete on-site [1,2]. This approach retains the benefits of traditional PC methods, such as a shorter construction time, reduced labor and material costs, and superior quality control, while also addressing the vulnerabilities of traditional PC structures, such as leakage and thermal problems at the joints and difficulty in ensuring the integrity between components [3–6].

Existing types of PC double walls can be categorized as shown in Figure 1. Table 1 summarizes the features of the four types of PC double walls presented in Figure 1. The PC truss wall (PTW) connects inner and outer panels with steel trusses [7], whereas the mega double wall (MDW) forms an integrated wall via a concrete connection between the inner and outer panels [8]. The stable, strong, and sustainable wall (3SW) is a double wall with vertical and horizontal reinforcing bars (rebars) placed between two panels. The vertical rebars connect the inner and outer panels, whereas the bent horizontal rebars (S-bars) are exposed at the joints to ensure improved integrity between the PC components and cast-in-place (CIP) concrete [9]. The I-wall differs from the previous PC wall systems as the PC panels are placed vertically and the connectors are constructed simultaneously, thus ensuring integrity between the two panels [10].

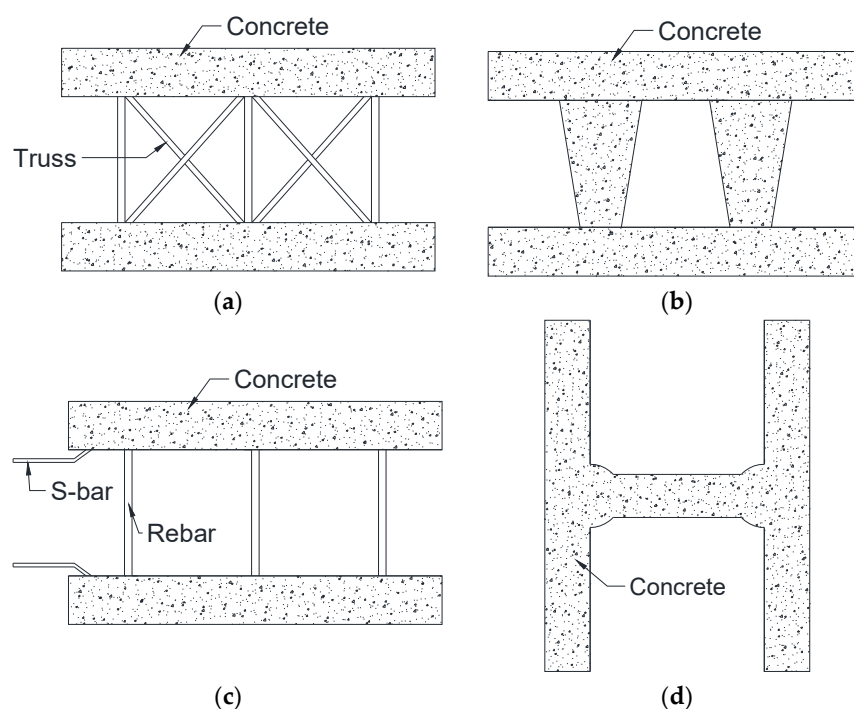


**Figure 1.** Description of PC double-wall types. (a) PTW (precast concrete truss wall); (b) MDW (mega double wall); (c) 3SW (stable, strong, and sustainable wall); (d) I-wall.

**Table 1.** Types of PC double walls.

	PTW	MDW	3SW	I-Wall
Components	(Slab + Truss) + Slab	(Slab + Con) + Slab	(Slab + Rebar) + Slab	Wall + Concrete + Wall
Mold complexity	Simple (mold for concrete panels only)	Complicated (mold for concrete panels and concrete joints)	Simple (mold for concrete panels only)	Complicated (mold for concrete panels and concrete joints)
Number of concrete casting procedures	2 (top slab + bottom slab)	2 (top slab + bottom slab)	2 (top slab + bottom slab)	1
Laitance	O	O	O	X
Integrity	Bond (angle steel + stud)	Connecting rebar	Bond (dowel)	Connecting rebar
Drawback	Cracking, low productivity	Cracking	Cracking, low productivity	Difficult demolding

Note: PTW—precast concrete truss wall, MDW—mega double wall, 3SW—stable, strong, and sustainable wall.

Many recent studies have focused on reducing the size and weight of PC double-wall systems [11,12], increasing the thermal resistance of the panels [13,14], and verifying the performance of PC double-wall systems to be utilized in irregular infrastructure such as apartment frameworks, balconies, stairs, railings, and underground parking lots [15–19]. However, few researchers have addressed the problems that occur during the manufacturing of PC double-wall systems [20].

A PC double-wall system consists of two PC panels manufactured in a factory, transported to the construction site, and filled with CIP concrete on-site. Therefore, it is crucial to ensure the integrity between the connection components or connecting steel and the PC panels to prevent any damage to the panels from unexpected loads during transportation or lateral pressure during CIP concrete placement [21]. The PC double-wall method developed in this study, as shown in Figure 2, aims to simplify the existing complex process of fabricating PC double-wall systems and eliminate defects like laitance that can occur during

the manufacture of concrete components. As the wall is erected vertically, laitance does not occur on the inner surfaces of the vertical panels. Furthermore, as the concrete is placed only once in standardized molds, defects are minimized and productivity is improved compared to traditional horizontal-placement PC double walls, which require flipping the PC components for concrete placement [10]. As shown in Figure 2, this system was developed to connect the PC panels using rectangular steel tubes and horizontal rebars within the panels, which serve as the connecting steel, penetrating the ends of the steel tubes and thus allowing for integrity via dowel action. However, the connection between the PC panels and connecting steel, as well as the attachment performance and overall integrity based on the embedded length, need to be clarified. In this study, 11 test specimens were fabricated for an experiment and finite element analysis (FEA). Figure 3 illustrates the potential failure modes when the rectangular steel tubes embedded in the PC panels resist direct tensile forces. According to the concrete structural design criteria provided by the Korean Design Standards Code [22], the potential failure modes when steel embedded in concrete resists tensile forces can be categorized into tensile failure of steel, pullout failure, and concrete breakout. In this study, the possibility of concrete side-bursting failure was excluded, assuming that the embedded length of the rectangular steel tube and the distance from the steel tube to the end of the concrete section are sufficient.

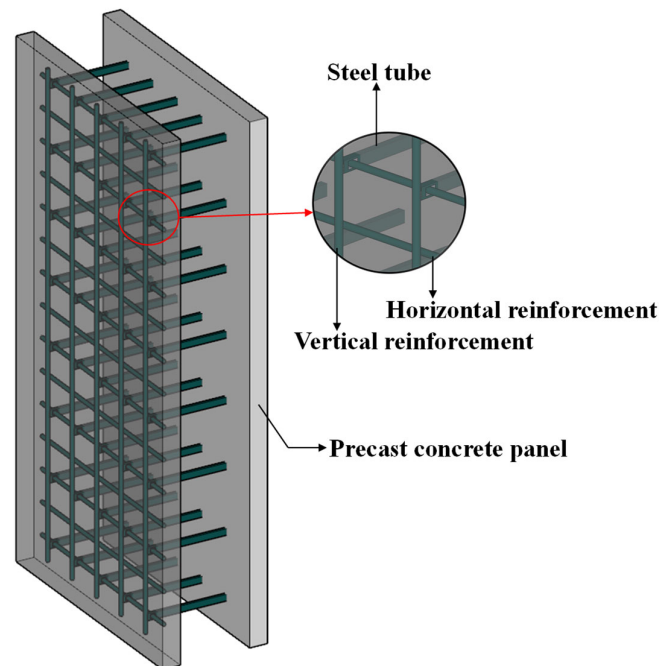


Figure 2. Description of the proposed double-wall system.

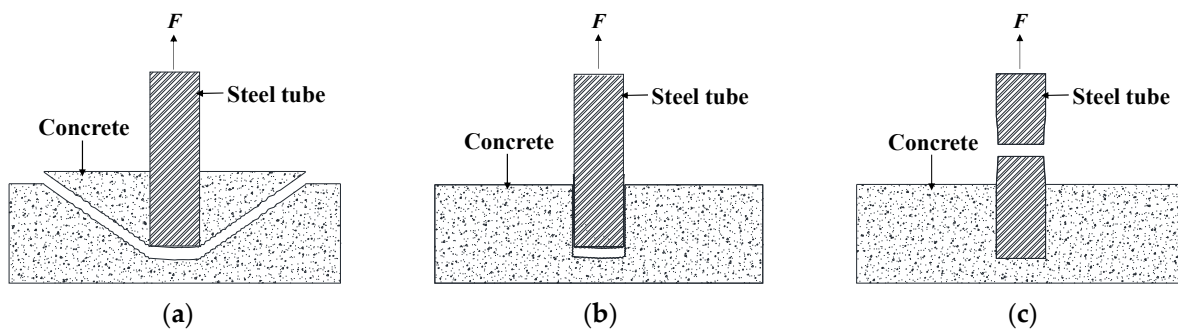


Figure 3. Failure modes between panel and steel tube. (a) Concrete breakout failure; (b) pullout failure; (c) steel-tube failure.

This study aimed to evaluate the tensile resistance performance of the connections in rectangular steel tubes, which are influenced by the dowel action of the horizontal rebar passing through the tubes, rather than verifying the bond strength between the steel tubes and concrete panel. A tensile test and FEA were conducted on the rectangular steel tubes to evaluate the end details of the steel tube, such as the presence of welded or bent steel plates and embedded concrete for securing dowel action. The findings of this study provide a comprehensive understanding of the structural performance of steel tubes with various tube end reinforcements under tension. Furthermore, the results of this study can be used in the development of the newly proposed PC double-wall system that simplifies the existing complex process of fabricating PC double-wall systems and eliminates defects like laitance that can occur during the manufacture of concrete components.

## 2. Experimental Scheme

### 2.1. Specimen Details

Steel tube types with 7 different connection details and lengths were designed and 11 test specimens were fabricated, including some with identical details so we could evaluate the tensile strength of the rectangular steel tubes through which horizontal rebars pass. The steel-tube type used for all test specimens was determined according to the general structural rectangular steel-tube standard [23]: SRT275 steel with a minimum yield and tensile strength of 275 MPa and 410 MPa was used. As shown in Figure 4, the total lengths of the rectangular steel tubes were 325 mm and 400 mm, with a width and height of 30 mm and 60 mm, respectively, and a nominal wall thickness of 3.2 mm. The ends of the rectangular steel tubes embedded in the PC panels were cut open, and high-strength bolts were connected to imitate the horizontal rebars that induce dowel effects through the opening. For the high-strength bolts, M16 was used as per the KS bolt standard [24]. The key variables of this experiment were the total length and the tube end details such as the presence of welded or bent steel plates and embedded concrete, as summarized in Table 2. The ST shown in Figure 4a was the control specimen, whose tube ends had the sides cut and removed. The ST\_CP, ST\_W1, ST\_W2, and ST\_CON specimens shown in Figure 4b–e were designed to effectively resist the dowel action force exerted by the bolts. The fabrication of ST\_CP involved bending a cut steel plate inward toward the end of the tube. ST\_W1 and ST\_W2 were manufactured by welding one and two steel plates inside the tube opening, respectively. Additionally, the ST\_CON specimen in Figure 4e was filled with concrete up to 90 mm from the tube end to simulate the composite steel–concrete resistance.

**Table 2.** Types of specimens.

Specimens	Variables		
	Opening Characteristics	Length (mm)	
ST	basic	325	400
ST_CP	curved plate	-	400
ST_W1	one-plate welding	325	400
ST_W2	two-plate welding	325	-
ST_CON	embedded concrete	325	-

### 2.2. Test Setup and Measurement

Figure 5 shows the test setup and measurement conducted in this study. A total of 11 specimens were tested using a universal testing machine (UTM) with a 1200 kN capacity, applying force at a displacement-controlled rate of 2 mm/min. As depicted in Figure 5, the upper part of the steel tube was secured with multiple layers of 9 mm thick steel plates bolted together. High-strength bolts were inserted into the openings of the tubes to apply tensile forces. A rectangular solid steel prism that filled the longitudinal hollow space of the steel tube was inserted into the lower part of the steel tube and fixed onto the UTM jig

to prevent local buckling at the tube end. Strain gauges were installed on both sides at the center of the height of the specimens to measure their vertical strains.

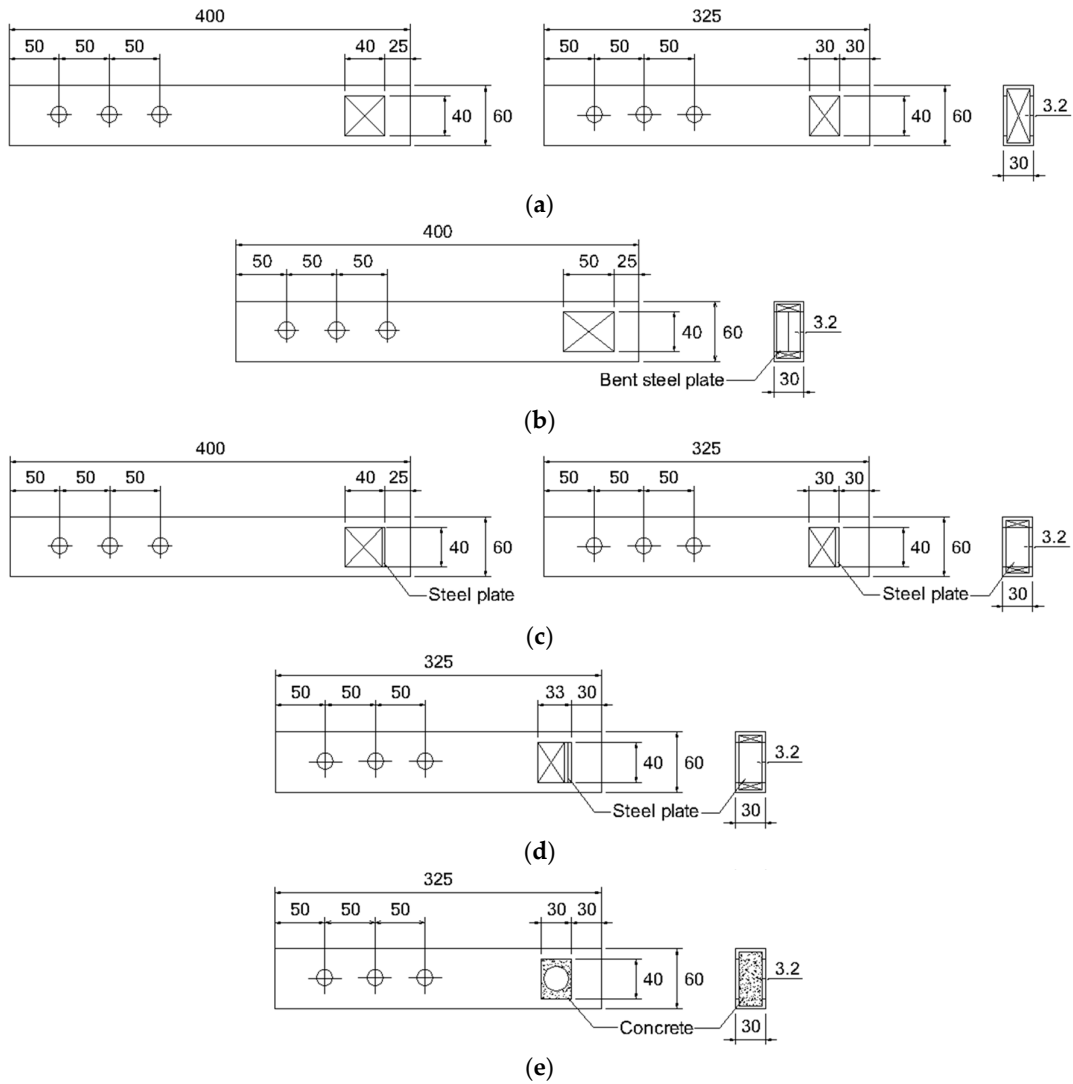


Figure 4. Specimen details (mm). (a) ST; (b) ST\_CP; (c) ST\_W1; (d) ST\_W2; (e) ST\_CON.

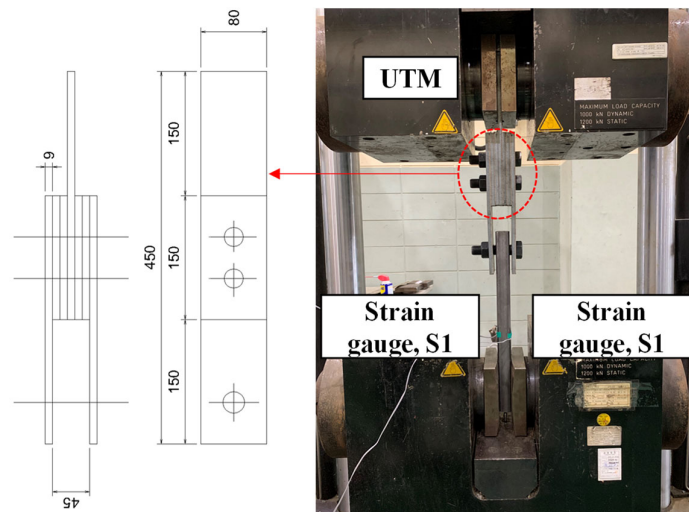


Figure 5. Experimental setup.

### 3. Experimental Results

Figure 6 shows the load–displacement curves for all the test specimens. Multiple specimens with identical characteristics were tested to ensure the reliability of the test results. Furthermore, Table 3 presents the maximum tensile strength and initial stiffness measured for the steel-tube specimens in the experiment.

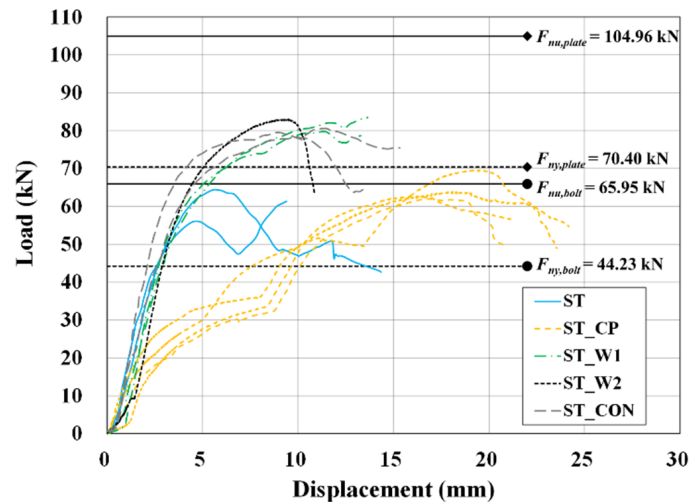


Figure 6. Experimental load–displacement results.

Table 3. Experimental and simulation results.

No.	Specimen	Experimental Results		Simulation Results		Nominal Strength	
		Tensile Strength (kN)	Initial Stiffness (MPa)	Tensile Strength (kN)	Initial Stiffness (MPa)	Yield Strength, $F_{ny}$ (kN)	Tensile Strength, $F_{nu}$ (kN)
1	ST_325	64.36	-	68.77	199,259	44.23	65.95
2	ST_400	61.33	200,315	56.57	199,633	(bolt)	(bolt)
3	ST_CP_400_1	61.97	204,740				
4	ST_CP_400_2	62.70	199,842			70.40	104.96
5	ST_CP_400_3	69.68	194,406	61.12	199,940	(plate)	(plate)
6	ST_CP_400_4	63.90	200,251				
7	ST_W1_325	79.74	284,174	80.01	199,251	70.40	104.96
8	ST_W1_400	83.47	196,953	81.08	199,487	(plate)	(plate)
9	ST_W2_325	83.05	282,960	84.14	201,393	70.40	104.96
						(plate)	(plate)
10	ST_CON_325_1	78.39	259,016			-	-
11	ST_CON_325_2	80.54	265,737	78.42	200,243		

Note: ST\_Variable\_X, X = specimen length.

The control specimen ST exhibited a maximum tensile strength at a load of 62.85 kN. The ST\_CP, ST\_W1, ST\_W2, ST\_CON, and ST\_REB specimens showed maximum tensile strength at loads of 61.97 kN, 81.61 kN, 83.05 kN, 79.47 kN, and 74.95 kN, respectively. Compared to the control specimen ST, the maximum tensile strength of the ST\_CP, ST\_W1, ST\_W2, and ST\_CON specimens increased by approximately 3%, 29%, 32%, and 26%, respectively. The ST\_CP specimens, with the steel-tube sides cut and bent, showed almost no increase in maximum tensile strength compared to the control specimen. The ST\_W1 and ST\_W2 specimens, with one and two layers of steel plates welded to the cut sides of the steel tubes, respectively, had the highest maximum tensile strength.

As shown in Figure 6, all specimens exhibited similar initial stiffness up to approximately 2 mm of displacement; however, a sudden drop in stiffness occurred in the ST\_CP specimen, for which the steel plate was cut from the side of the steel-tube end and bent inward. The stiffness was significantly lower in this specimen because the steel plates were plastically deformed due to bending to resist the tensile force introduced by the bolt. According to Choi et al. [25], the yield and maximum tensile strength of bent rebars are lower than those of unbent rebars, leading to fractures at the bent portion of the rebar.

Table 3 shows the strength of the specimens compared to their nominal strength as calculated using their yield and tensile strength. The strength of each specimen was determined by using the smallest value between the tensile yield, tensile fracture, and crushing of the steel tube due to the bolt. In this experimental study, the strength of the specimens was determined considering the bearing force exerted by high-strength bolts, because the cross-sectional area subjected to this bearing force was the smallest. For specimens reinforced with steel plates that were either bent or cut at the longitudinal hollow section, additional resistance was expected due to the reinforced steel plate in addition to the bearing force exerted by high-strength bolts. Therefore, the area used to calculate nominal strength was adjusted differently, considering the bearing area influenced by the semicircle of the high-strength bolt and the length of the cut area. Accordingly, the nominal yield strength ( $F_{ny}$ ) and nominal tensile strength ( $F_{nu}$ ) were, respectively, calculated as

$$F_{ny} = A_e f_y \quad (1)$$

$$F_{nu} = A_e f_u \quad (2)$$

where  $A_e$  represents the effective bearing area, calculated as  $\varphi\pi/2 \times 2t_s$ , for the case of high-strength bolts. For steel-plate reinforcement, as shown in Figure 4,  $A_e$  was determined considering that the length of the reinforced steel plate was 40 mm, thus  $40 \times t_s$ . Moreover,  $\varphi$  represents the diameter of the high-strength bolts and  $t_s$  denotes the thickness of the rectangular steel tube.  $f_y$  and  $f_u$  are the yield and tensile strength of the rectangular steel tube, respectively. To calculate the design's nominal strength, the minimum yield and tensile strength (275 MPa and 410 MPa) specified by KS for SRT275 were used. Therefore, in Table 3, the nominal yield strength ( $F_{ny\_bolt}$ ) and nominal tensile strength ( $F_{nu\_bolt}$ ) due to bolt bearing force, as well as the nominal yield strength ( $F_{ny\_plate}$ ) and nominal tensile strength ( $F_{nu\_plate}$ ) due to the reinforced steel plate, are presented. However, nominal strength is not indicated for the ST\_CON series with concrete-filled reinforcement, as their strength cannot be evaluated using the same method.

According to Figure 6, all specimens exhibited a strength greater than the nominal yield strength due to bolt bearing force ( $F_{ny\_bolt}$ ), although the ST and ST\_CP specimens showed a lower strength than the nominal tensile strength due to bolt bearing force ( $F_{nu\_bolt}$ ). Other specimens showed a strength exceeding the nominal yield strength due to the reinforced steel plate ( $F_{ny\_plate}$ ) but failed to reach the nominal tensile strength imparted by the reinforced steel plate ( $F_{nu\_plate}$ ). Therefore, these results indicate that steel-plate reinforcement provides sufficient additional resistance to achieve the nominal yield strength ( $F_{ny\_plate}$ ).

In the experimental study, the total length of the steel tube varied, in addition to the details of the ends of the tubes. The ST and ST\_W1 specimens were fabricated in two lengths: 325 mm and 400 mm. The ST specimens exhibited a maximum tensile strength of 64.36 kN and 61.33 kN for each length, whereas ST\_W1 specimens showed a maximum tensile strength of 79.74 kN and 83.47 kN. Therefore, these results indicate no significant correlation between the total length of the specimen and its maximum tensile strength. Table 3 shows the experimental initial stiffness calculated from the stress–strain results of the specimens. The stress was calculated by dividing the tensile force measured according to the cross-sectional area of the steel tube. The strain was derived from the strain gauges attached to the center of all specimens. The strain obtained from the strain gauges in all specimens did not reach the typical yield strain of conventional steel materials

(0.002~0.0025), possibly because the location where the strain gauge was attached was distant from the point of failure of the specimen. For the 325 mm specimens, an average initial stiffness of 272,972 MPa was observed, whereas the 400 mm specimens showed an average initial stiffness of 199,836 MPa. The strain gauge of the ST\_325 specimen was damaged during the experiment; thus, it was excluded from Table 3. Strain gauges were attached to the middle of the specimens regardless of their length; however, stress and strain would be concentrated around the failure points near the openings. Thus, openings in the connection details significantly influence the tensile performance of rectangular steel tubes.

Excluding the ST\_CP specimens, all specimens demonstrated a strength improvement of over 20% compared to the control specimen ST. If ST\_W1 or ST\_W2 is used for connecting steel details, additional construction steps and costs will be incurred in welding steel plates to the rectangular steel tubes before fabricating the PC panels. However, ST\_CON, which involves filling the inside of the steel tube with concrete, requires no additional construction steps or costs during the PC double-wall production process, thus making it a feasible option for steel-tube end details during the manufacture of PC panels. Therefore, considering both the strength and construction procedure, ST\_CON is regarded as the most suitable steel-tube end detail for the PC double-wall system.

#### 4. Finite Element Analysis

The finite element analysis (FEA) of the steel-tube specimens was established using Abaqus/Static General considering nonlinear geometry effects. The FEA models followed the dimensional details of the specimens in the experiment. The 3D model of the specimens consisted of steel tube, bolt, plate, and concrete depending on the steel-tube type.

##### 4.1. Constitutive Material Models

###### 4.1.1. Steel

The material model of the steel tubes and plates consisted of three parts in this paper: the elastic part, plastic part, and ductile damage part. The ductile damage initiation criterion is a model that predicts the damage caused by the nucleation, growth, and aggregation of voids when the steel structural members undergo large plastic deformation [26]. With the introduction of the damage evolution ability in ductile damage, the material hardness of steel structural members gradually degrades, leading to material failure and element deletion. The following equations show brief mathematical expressions for the three parts of the material model in the FEM [26,27]:

$$\sigma_i = \begin{cases} E \times \varepsilon & \left( \varepsilon \leq \varepsilon_y \right) \\ f_y + E_1 \times (\varepsilon - \varepsilon_y) & \left( \varepsilon > \varepsilon_y \right) \end{cases} \quad (3)$$

$$\sigma = (1 - D)\bar{\sigma} \quad (4)$$

where  $\sigma_i$  is the stress of the element in FEA up to the necking,  $\sigma$  is the stress of the element in FEA at the necking,  $E$  is the elastic modulus of the steel,  $E_1$  is the strengthening coefficient of the steel entering the plastic stage,  $\varepsilon_y$  is the yield strain of the steel,  $f_y$  is the yield stress of the steel,  $D$  is the overall damage variable, and  $\bar{\sigma}$  is the stress that exists in the undamaged material. The material properties of the steel tube were assigned referring to the material test results shown in Figure 7.

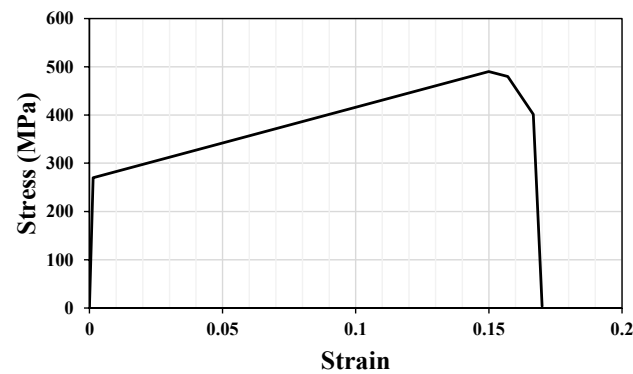


Figure 7. Material properties of the steel.

#### 4.1.2. Concrete

The concrete damage plasticity (CDP) model was assigned to concrete for the ST\_CON specimen. The CDP model considers the inelastic behavior of concrete by defining damage factors in both compression and tension [28]. The stress–strain relationships of concrete were assigned referring to the material test results shown in Figure 8. For the damaged part’s input parameters in the CDP model, the recommended values for the concrete materials used in a steel–concrete composite girder in the existing study [29,30] were used, as presented in Table 4.

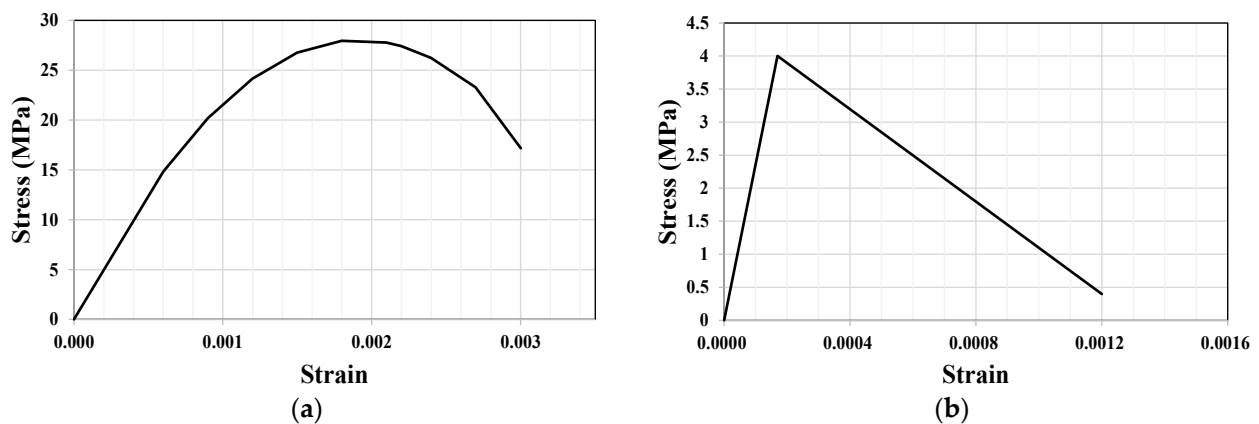


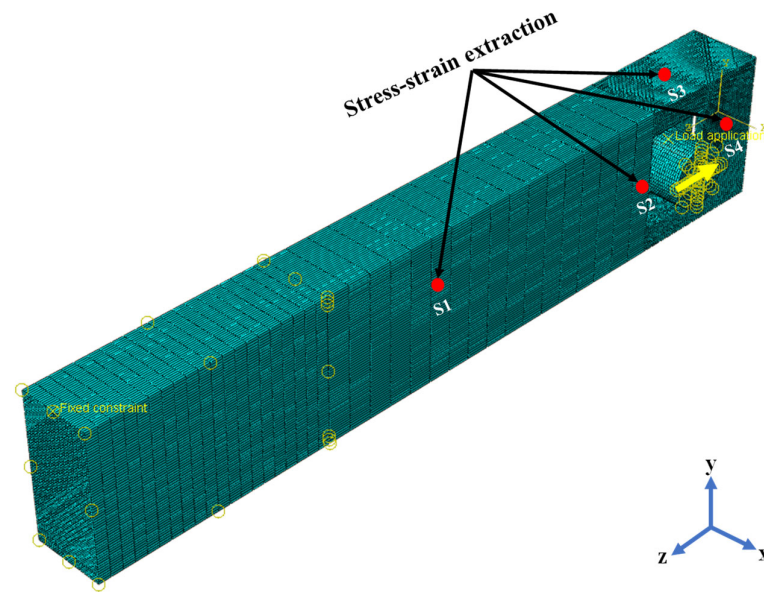
Figure 8. Material properties of the concrete. (a) Compressive strength; (b) tensile strength.

Table 4. Input parameters for the concrete damage plasticity model.

Dilation Angle (Degree)	Eccentricity	$f_{b0}/f_{c0}$	K	Viscosity Parameter
38	0.1	1.16	0.6667	0

#### 4.2. Boundary Condition, Contact Mode, and Mesh

For the steel-tube specimens, the bolt was inserted inside the opening of the steel tube to apply the tensile force. The bolt and lower end of the steel tube, which is opposite to the loading end, were defined as the rigid body by connecting the reference points to them, as shown in Figure 9. The lower end of the steel tube was fixed in all degrees of freedom, while displacement in the z-direction was applied by the bolt.



**Figure 9.** Boundary conditions and mesh of the model.

The interfacial contact between the steel tube and bolt was defined as a hard contact in a normal direction and friction contact in a tangential direction with a frictional coefficient of 0.2 for the control specimen ST. For the ST\_W1 and ST\_W2 specimens, steel plates with one and two layers were located inside the opening of the steel tubes, respectively, and a tie constraint was added between the steel-plate and steel-tube opening surfaces to imitate welding. For the ST\_CP specimen that had cut and bent sides, the lower material properties at the bent surface were assigned in the model to imitate residual stress after bending. For the ST\_CON specimen, the shear stress limit was introduced in the contact property definition to ensure bonding between the steel tube and the inside concrete. The idea behind the shear stress limit is that it allows the shear stress for the interface between the steel tube and inside concrete to be transferred if the shear stress is not greater than the critical value of the interface bond stress. However, relative slip will occur between the steel tube and inside concrete when the value of shear stress is greater than the critical interface bond stress [27,31], as expressed in Equation (5):

$$\tau = \mu p \begin{cases} \leq \tau_{bond} & (\text{coordination deformation}) \\ > \tau_{bond} & (\text{relative slip}) \end{cases} \quad (5)$$

where  $\tau$  is the shear stress,  $\tau_{bond}$  is the critical interface bond stress, taken as 1.0 MPa,  $\mu$  is the friction coefficient of 0.2, and  $p$  is the pressure of interfacial contact.

Figure 9 shows the mesh of the model. A structured hexahedral element shape mesh C3D8R was implemented for the steel tube and a sweep hex-dominated element shape mesh C3D6 was implemented for the bolt. There were two mesh sizes used for the steel-tube model. In the section near the steel-tube opening, a fine mesh of 1 mm was created, while in the other sections, a coarse mesh of 11 mm was created. A suitable mesh size at the steel-tube opening section was selected by conducting a mesh convergence study. The convergence study started with a coarser mesh of 8 and subsequently was subdivided until the convergence issue was overcome and the error between simulation and experimental results was within the 5% tolerance. Figure 10 shows the results of the convergence mesh study for the ST\_325 specimen. The mesh size of the bolt was made larger than the steel-tube opening to prevent penetration due to the master and slave surface contact.

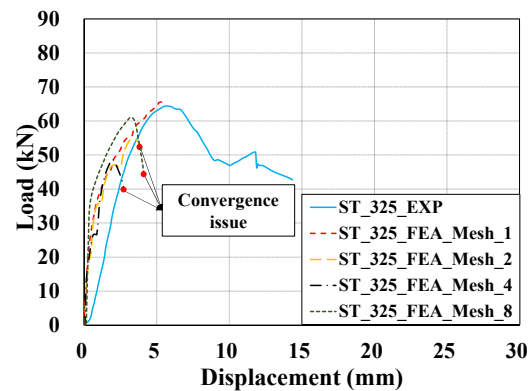


Figure 10. Mesh convergence study results for the ST specimen.

## 5. Discussion

### 5.1. Verification of the Simulation Results

FEA of seven different steel-tube types in terms of the total length and tube end details was conducted by adopting the above modeling methods and material models. The comparison of the load–displacement curves of the simulation and experimental results along with FEA failure modes is shown in Table 3 and Figure 11. The tensile strength capacities obtained in the experiment and simulation are similar, as shown in Table 3. In general, all the results are in acceptable agreement for all specimens, with a maximum error of 7.6% between the simulation and experimental results, which proves the reliability of the simulation results.

### 5.2. Contributions of Tube End Reinforcements

The failure modes of the specimens were well captured by the simulation. From the stress distribution of the FEA models in Figure 11, it can be noticed that in the ST\_325 and ST\_400 specimens, the region around the steel-tube opening and steel-tube end was subjected to higher stress, while the damage initiation process began at the interaction region between the steel-tube opening and rigid bolt.

The load–displacement relationship of the ST\_CP specimen had two connected curves, which indicates two phases of failure mode. In the first phase, the tensile load was resisted by the bent steel plates up to 8.1 mm. Since the bent region of the steel plates was the weakest part of the model considering the residual stress, the connection between the bent steel plates and steel tube was lost when the steel at the bent region was damaged, and in the second phase, the tensile load was resisted by the thin walls of the steel tube only.

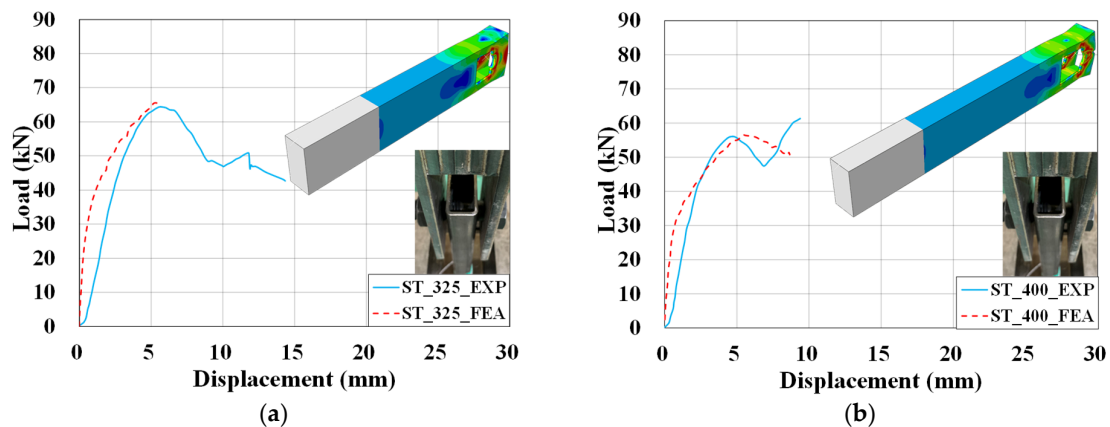


Figure 11. Cont.

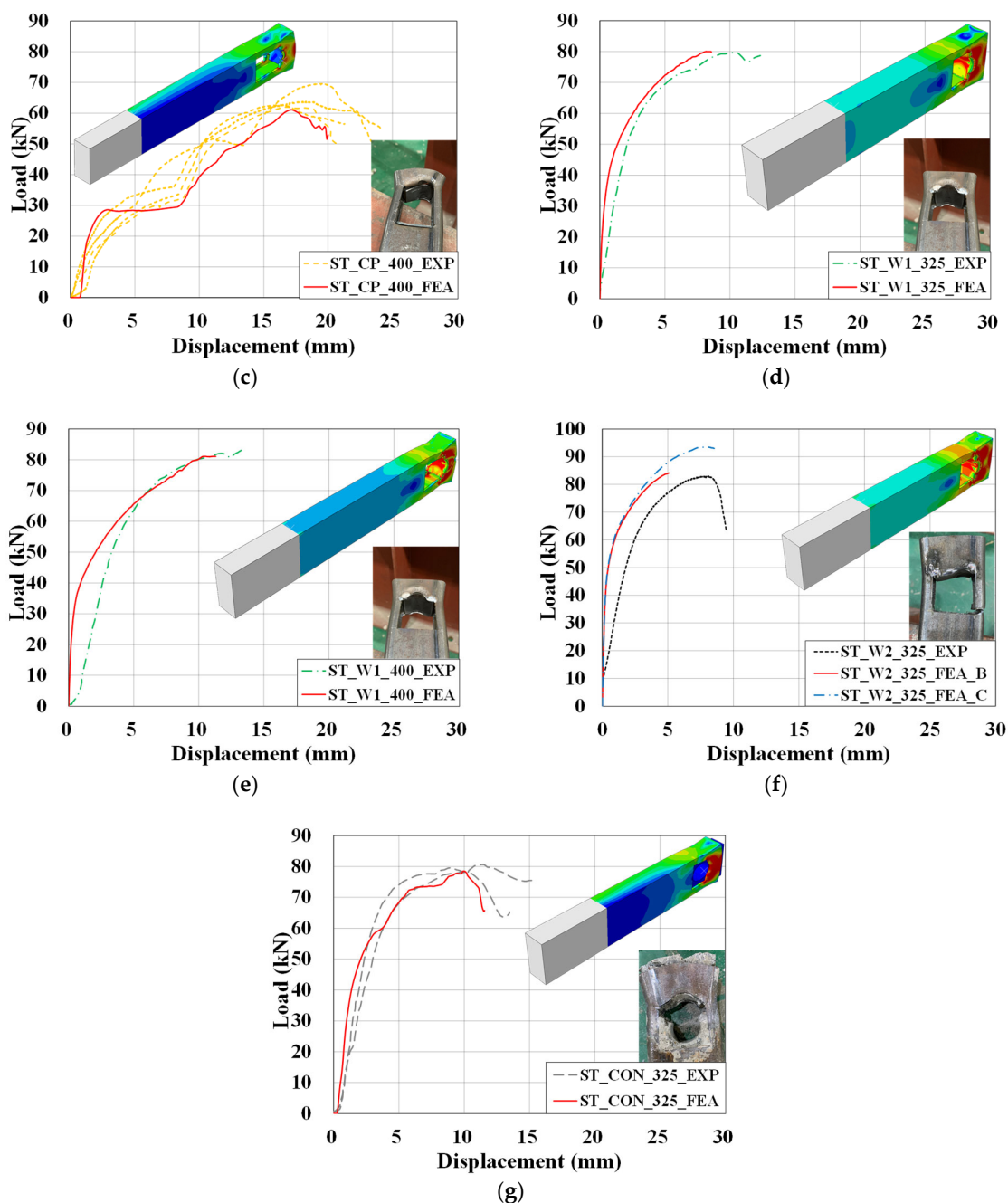


Figure 11. Comparison of the experimental and FEA results with failure modes. (a) ST\_325; (b) ST\_400; (c) ST\_CP\_400; (d) ST\_W1\_325; (e) ST\_W1\_400; (f) ST\_W2\_325; (g) ST\_CON\_325.

Regarding the ST\_W1 and ST\_W2 specimens, welded steel plates actively participated in the tensile load resistance, and the tensile strength of the specimens increased by 29% and 32% in comparison with the control specimen, respectively. During the experiment for the ST\_W2 specimen, the bolt applying tensile load moved to the right side, leading to asymmetrical loading. As a result, the specimen ST\_W2 broke through the width of the steel tube, as presented in Figure 11f. Due to this, there was a trivial difference in the tensile strength between the ST\_W1 and ST\_W2 specimens, and the contribution of the welded steel plates was not fully determined. Figure 11f shows two simulation results for the ST\_W2 specimen. The dashed blue line represents the bolt load applied from the center of the steel-tube opening, while the red line represents the bolt load applied from the bottom side of the steel-tube opening. After changing the location of the bolt from

the center to the bottom, the tensile strength of the steel tube decreased from 93.46 kN to 84.14 kN, a 10% decrease. Therefore, the tensile strength of the steel tube could be influenced by the load-applying location. For the ST\_CON specimen, the contribution of the embedded concrete to the resistance of the tensile load was significant at the early stage of the load–displacement behavior. However, due to the bond–relative slip definition, the contribution of the concrete became insignificant after 5 mm, and most of the tensile load was resisted by the steel in the steel–concrete composite.

As indicated in Figure 9, the stress–strain data were derived from four mesh points in the finite element model. The first point (FEA\_S1) corresponds to the location of the strain gauge in the experiment (EXP\_S1), which is the middle point from the total span length of the steel tube. The second point (FEA\_S2) is located in the middle of the left end of the steel-tube opening. The third point (FEA\_S3) is located in the middle of the steel-tube opening from the top side. The fourth point (FEA\_S4) is in the middle between the right end of the steel-tube opening and the end of the steel tube. Figure 12 shows the stress–strain curves obtained from the experimental and FEA results. Points S1, S2, and S3 experienced tensile strain, while S4 experienced compressive strain. For all specimens, the hierarchy of the strain development ranged from S1 to S4, implying that higher strains were developed at the locations close to the region of the load application. The experimental stress–strain curves for short specimens having a total length of 325 mm had different stiffness values than seen in the FEA results, as shown in Table 3 and Figure 12. The reason for this deviation is the use of two different stress calculation methods. The experimental stress results were derived by dividing the load by the cross-sectional area, while the FEA stress results were obtained from the mesh element, which follows the assigned steel material properties shown in Figure 7. Despite this, the experimental strain results and FEA strain results for the first point (S1) are almost identical, highlighting the validity of the FEA simulation results.

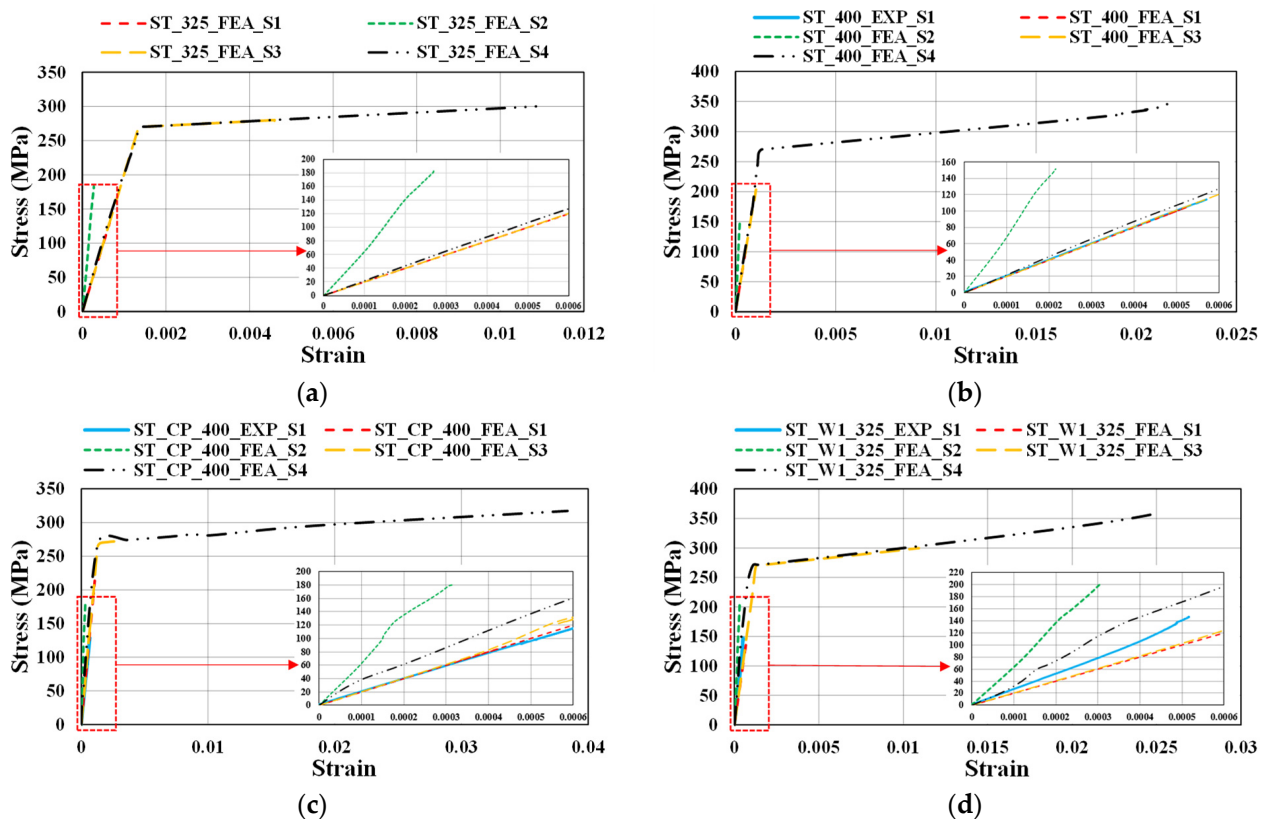
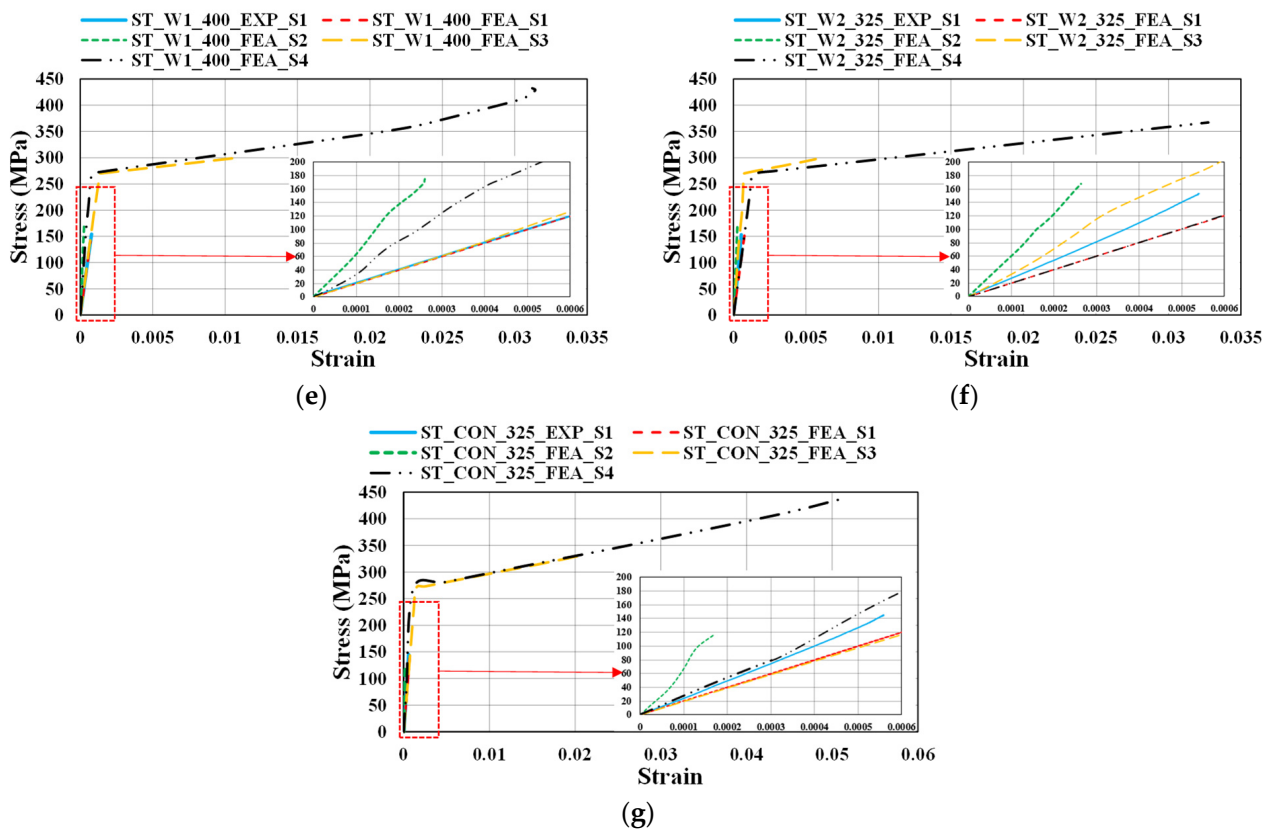


Figure 12. Cont.



**Figure 12.** Comparison of the experimental and FEA stress–strain curves. (a) ST\_325; (b) ST\_400; (c) ST\_CP\_400; (d) ST\_W1\_325; (e) ST\_W1\_400; (f) ST\_W2\_325; (g) ST\_CON\_325.

## 6. Conclusions

This study introduced a developed PC double-wall system and performed experiments and finite element analysis to evaluate the direct tensile capacity of the steel-tube connections due to the dowel action of the horizontal rebar. Based on the experiment, FEA results, and constructability, the most suitable end details for the rectangular steel tubes in the developed PC double-wall system were determined. The conclusions derived from this study are as follows:

- (1) Rectangular steel-tube specimens reinforced with welded steel plates (ST\_W1 & ST\_W2) and concrete infill (ST\_CON) achieve maximum tensile strength increases of approximately 20–32% compared to the baseline specimen (ST), without reinforcement in the hollow section.
- (2) Specimens with a steel plate cut and bent inward at the tube end (ST\_CP) did not exhibit an increased maximum tensile strength compared to the control specimen (ST) because for ST\_CP, the steel plate, which endured plastic deformation due to bending, failed to contribute to an increase in maximum tensile strength.
- (3) The length of the rectangular steel-tube specimens does not significantly affect strength.
- (4) ST\_CON is the most suitable connection as it does not require additional construction steps or costs compared to other connection details. The specimen has similar details to the rectangular steel-tube connection used in the PC double-wall system and involves filling the hollow section of the rectangular steel-tube specimen with concrete.

Future research is needed to clarify the varying performance of PC double-wall connections. Particularly, an in-depth examination of the performance of steel-tube connections embedded in PC panels is necessary, addressing potential issues such as steel-tube pullout failure, concrete breakout failure, and material failure of the steel tubes.

**Author Contributions:** Conceptualization, H.J.; methodology, Y.S.; validation, D.M. and H.J.; investigation and data curation, Y.S. and H.-C.C.; writing—original draft preparation, D.M. and Y.S.; writing—review and editing, D.M. and H.J.; supervision, H.J.; funding acquisition, H.-C.C. and H.J. All authors have read and agreed to the published version of the manuscript.

**Funding:** This work was supported by the Technology Development Program (S3276632) funded by the Ministry of SMEs and Startups (MSS, Republic of Korea).

**Data Availability Statement:** The data presented in this study are available on request from the corresponding authors. The data are not publicly available due to privacy.

**Conflicts of Interest:** Author Hae-Chang Cho was employed by the company Dream Structural Engineers Co., Ltd. The remaining authors declare that the research was conducted in the absence of any commercial or financial relationships that could be construed as a potential conflict of interest.

## References

1. Oh, Y.H.; Moon, J.H.; Kim, J.K.; Lee, J.H.; Shin, S.H. Evaluation of Structural Performance for Precast Concrete Double-wall with Different Aspect Ratios and Joint Rebar Ratios. *J. Korea Concr. Inst.* **2020**, *32*, 445–455. [\[CrossRef\]](#)
2. Lee, W.J.; Kim, M.; Lee, D.; Ju, H.; Kim, K.H. Seismic Performance Evaluation of Intermediate Precast Structural Walls. *J. Next-Gener. Converg. Technol. Assoc.* **2022**, *6*, 421–432.
3. Kim, S.; Lee, D.E.; Kim, Y.; Kim, S. Development and application of precast concrete double wall system to improve productivity of retaining wall construction. *Sustainability* **2020**, *12*, 3454. [\[CrossRef\]](#)
4. Gleich, H. *New Carbon Fiber Reinforcement Advances Sandwich Wall Panels*; Structure Magazine: Chicago, IL, USA, 2007; pp. 61–63.
5. Kim, Y.J.; Allard, A. Thermal response of precast concrete sandwich walls with various steel connectors for architectural buildings in cold regions. *Energy Build.* **2014**, *80*, 137–148. [\[CrossRef\]](#)
6. O’Hegarty, R.; Reilly, A.; West, R.; Kinnane, O. Thermal investigation of thin precast concrete sandwich panels. *J. Build. Eng.* **2020**, *27*, 100937. [\[CrossRef\]](#)
7. Oh, Y.H.; Moon, J.H. *Evaluation Study on the Integral of the PC and the RC of the MDW Method*; Korea Concrete Institute: Seoul, Republic of Korea, 2017; pp. 1–36.
8. Ji, K.H.; Choi, B.J. Improvement of Underground Wall Design and Construction Safety Using Mega Double Wall Construction Method. *J. Korean Soc. Hazard Mitig.* **2019**, *19*, 1–12. [\[CrossRef\]](#)
9. Park, Y.S. PC DW: Precast Double Wall, 3SW: Stable, Strong, Sustainable. *J. Korea Concr. Inst.* **2021**, *33*, 59–61.
10. Seo, Y.; Ju, H. Evaluation of Steel Tube Connection in Precast Concrete Double Wall System. *J. Korea Inst. Struct. Maint. Insp.* **2023**, *27*, 25–32.
11. Hegger, J.; Zell, M.; Horstmann, M. Textile Reinforced Concrete—Realization in applications. In Proceedings of the 2008 International FIB Symposium, Amsterdam, The Netherlands, 19–21 May 2008.
12. Bramshuber, W. *Report 36: Textile Reinforced Concrete—State-of-the-Art Report of RILEM TC 201-TRC*; RILEM Publications: Aachen, Germany, 2006.
13. Lee, B.-J.; Pessiki, S. Revised zone method R-value calculation for precast concrete sandwich panels containing metal wythe connectors. *PCI J.* **2008**, *53*, 86–100. [\[CrossRef\]](#)
14. Woltman, G.; Noel, M.; Fam, A. Experimental and numerical investigations of thermal properties of insulated concrete sandwich panels with fiberglass shear connectors. *Energy Build.* **2017**, *145*, 22–31. [\[CrossRef\]](#)
15. Augusto, T.; Mounir, K.; Melo, A.M. A cost optimization-based design of precast concrete floors using genetic algorithms. *Autom. Constr.* **2012**, *22*, 348–356.
16. Castilho, V.C.; Lima, M.C.V. Comparative costs of the production, transport and assembly stages of prestressed precast slabs using genetic algorithms. *Int. J. Optim. Civil Eng.* **2012**, *2*, 407–422.
17. Ko, C.H. Material transshipment for precast fabrication. *J. Constr. Eng. Manag.* **2013**, *19*, 335–347. [\[CrossRef\]](#)
18. Sacks, R.; Eastman, C.M.; Lee, G. Parametric 3D modeling in building construction with examples from precast concrete. *Autom. Constr.* **2004**, *13*, 291–312. [\[CrossRef\]](#)
19. Suh, J.I.; Park, H.G.; Hwang, H.J.; Im, J.H.; Kim, Y.N. Development of PC double wall for staircase construction. *J. Korea Inst. Build. Constr.* **2014**, *14*, 571–581. [\[CrossRef\]](#)
20. O’Hegarty, R.; Kinnane, O. Review of precast concrete sandwich panels and their innovations. *Constr. Build. Mater.* **2020**, *233*, 117145. [\[CrossRef\]](#)
21. Kim, H.D.; Lee, S.S.; Park, K.S.; Bae, K.W. A study on plant certification program for precast concrete products. *J. Korea Inst. Struct. Maint. Insp.* **2014**, *18*, 131–138. [\[CrossRef\]](#)
22. *KDS 14 20 54*; Standard for Durability Design of Concrete Structures. Korea Concrete Institute: Seoul, Republic of Korea, 2021.
23. *KS D 3568*; Carbon Steel Square Pipes for General Structural Purposes. Korea Agency for Technology and Standards: Seoul, Republic of Korea, 2018.
24. *KS B 1002*; Hexagon Head Bolts and Hexagon Head Screws. Korea Agency for Technology and Standards: Seoul, Republic of Korea, 2021.

25. Choi, H.B.; Kim, H.S.; Seo, D.S.; Kang, K.I. The study on the capability transform and alternative plan of reinforcing bar with straightening after bending. *J. Archit. Inst. Korea* **2003**, *19*, 181–188.
26. Li, F.; Yuan, H.; Liu, H. Implementation of metal ductile damage criteria in Abaqus FEA. In Proceedings of the 2021 IOP 4th International Conference on Advanced Materials, Intelligent Manufacturing and Automation (AMIMA), Hangzhou, China, 2–4 April 2021.
27. Bai, W.; Li, Y.; Ji, J.; Liu, Y.; Zhang, L.; Wang, R.; Jiang, L.; He, L. Axial Compression Behavior of Symmetrical Full-Scale Concrete Filled Double Skin Steel Tube Stub Columns. *Symmetry* **2022**, *14*, 223. [[CrossRef](#)]
28. Qingfu, L.; Wei, G.; Yihang, K. Parameter calculation and verification of concrete plastic damage model of ABAQUS. In Proceedings of the 2019 IOP International Conference on Architecture, Civil and Hydraulic Engineering (ACHE), Guangzhou, China, 20–22 December 2019.
29. Hibbitt, H.; Karlsson, B.; Sorensen, P. *Abaqus Analysis Users Manual, Version 6.10*; Dassault Systemes Simulia: Providence, RI, USA, 2011.
30. Ju, H.; Lee, D.; Choi, D. Finite element analysis of steel-concrete composite connection with prefabricated permanent steel form. *J. Asian Concr. Fed.* **2022**, *8*, 1–15. [[CrossRef](#)]
31. Dai, X.; Lam, D. Numerical modelling of the axial compressive behavior of short concrete-filled elliptical steel columns. *J. Constr. Steel Res.* **2010**, *66*, 931–942. [[CrossRef](#)]

**Disclaimer/Publisher’s Note:** The statements, opinions and data contained in all publications are solely those of the individual author(s) and contributor(s) and not of MDPI and/or the editor(s). MDPI and/or the editor(s) disclaim responsibility for any injury to people or property resulting from any ideas, methods, instructions or products referred to in the content.